



# Manufacturing of 3D Microlens Array Mold on Bulk Metallic Glass by Self-Aligned Multi-Ball Hot Embossing

Xiaohua Liu<sup>1,2</sup> · Ruodong Mo<sup>1</sup> · Kangsen Li<sup>1</sup> · Jun Shen<sup>1</sup> · Jiang Ma<sup>1</sup> · Feng Gong<sup>1</sup>

Received: 10 May 2020 / Revised: 24 August 2020 / Accepted: 1 September 2020  
© Korean Society for Precision Engineering 2020

## Abstract

Bulk metallic glasses (amorphous alloys) exhibiting both high hardness and extraordinary thermoplastic forming ability, are perfect mold material for 3D optical microlens array. However, conventional 3D micro fabrication for metallic glass requires Si templates which are extremely costly and eco-unfriendly to machine and demold. In this study, we report a green and low-cost self-aligned multi-ball hot embossing process to create 3D micro dimple array on metallic glass by replicating spherical crowns of self-aligned precision balls. A 3D metallic glass micro dimple array with aperture of 867.2  $\mu\text{m}$  and surface roughness of 8.2 nm was fabricated in 30 s. Different from conventional hot embossing that material full-filled into mold, the new process enables micro dimple fabrication with different specifications by freely controlling the down displacement of balls. Therefore, the relationship between down displacement and depth of micro dimple was revealed through exploring the material flow behavior by a verified FE model. In addition, to test the feasibility of the fabricated metallic glass mold, a PMMA compound eye structure was embossed and its focusing and imaging performance were subsequently evaluated. This research demonstrates a new manufacturing process for rapid fabrication of 3D microlens arrays metallic glass mold in a neat and economic way.

**Keywords** Bulk metallic glass · 3D microlens array mold · Self-aligned multi-ball hot embossing · Material flow behavior

## 1 Introduction

Bulk metallic glasses (BMGs) possess excellent mechanical properties including extremely high specific strength [1], super wear and corrosion resistance [2] as well as low elastic modulus with large elastic limit [3], which have aroused extensive interests since they were firstly prepared by Klement et al in 1960 [4]. Despite these remarkable engineering features, BMGs are especially known for their excellent

formability in the supercooled liquid region, which enables efficient and environment-friendly thermoplastic forming of metallic glasses like polymers or oxide glasses [5]. Benefiting from this ability, unlike general hard material processed by material removal methods such as etching and precision cutting, BMGs are capable of being plastically deformed into complicated multi-functional macro/micro/nano-structures with accurate geometry and shape because they intrinsically get rid of grain size limitations [6].

During the last decades, many studies on the thermoplastic forming of metallic glass microparts and microdevices have been reported aiming at exploring new functions and applications for microstructure patterns on metallic glass surfaces [7]. For example, Lee et al. [8] continuously fabricated metallic micromesh patterns on a flexible substrate to achieve the scalable fabrication of a novel transparent heater architecture. Li et al. [9] reported a honeycombed nanoporous/glassy structure on metallic glass surfaces as electrocatalyst, which can provide more active sites and contact areas for electrocatalytic reactions, promote charge transfer and electrolyte penetration, and increase hydrogen evolution reaction rates. Ida et al. [10] demonstrated the feasibility

✉ Jiang Ma  
majiang@szu.edu.cn

✉ Feng Gong  
gongfeng186@163.com

<sup>1</sup> Guangdong Provincial Key Laboratory of Micro/Nano Optomechatronics Engineering, College of Mechatronics and Control Engineering, Shenzhen University, Shenzhen 518060, China

<sup>2</sup> Key Laboratory of Optoelectronic Devices and Systems of Ministry of Education and Guangdong Province, College of Physics and Optoelectronic Engineering, Shenzhen University, Shenzhen 518060, China

of  $Zr_{70}Ni_{16}Cu_6A_{18}$  bulk metallic glass as a newly-developed biomaterial for implants fabrication. Liu et al. [11] proposed a cheap and rapid die nanoembossing technique for metallic glassy nanowire arrays to achieve high surface Raman scattering enhancement factor in optical system.

Among these studies, one of the most intriguing applications of metallic glasses with delicate surface patterns is the high precision mold for polymeric microstructures. Precision hot embossing and imprinting for microstructures and surface textures is a low-cost and widely used process for high volume and energy-saving production [12–15]. Polymeric microstructures, particularly 3D microlens arrays (also known as artificial compound eyes) are expected to achieve an extremely large field of view and high precision imaging with a compact volume [16]. To prolong the lifetime of molds and improve the geometrical accuracy of molded 3D microlens array, the molds used in molding are required to possess super hard and anti-corrosion properties in material and optical surface finish on micro dimple surfaces. Compared with other mold material, metallic glasses inherently have smooth and shiny surface finish and are much easier to fabricate microstructures due to their perfect replication capacity in supercooled liquid region [17]. Therefore, replicating microfeatures from another template to metallic glasses, becomes the most common approach to process metallic glass products with complex microstructures like micro dimple arrays. Zhang et al. [18] fabricated BMG tools through thermoplastic forming process with typical microfluidics patterns and features. Liu et al. [19] used silicon as template to accurately emboss inexpensive and durable  $Ni_{62}Pd_{19}Si_2P_{17}$  samples with complex large-area structures. Ma et al. [20] fabricated cylinder arrays and grating arrays on Pd-based metallic glass mold insert by embossing from a silicon mold during its supercooled liquid region. In Saotome et al.'s work [21], V-groove dies in range of 100 nm–1 mm were fabricated on a silicon template and then copied onto  $Pt_{48.75}Pd_{9.75}Cu_{19.5}P_{22}$  metallic glass surfaces.

However, traditional embossing of metallic glasses, which requires precise hard material templates such as Si, has two main drawbacks. One is that microstructures on Si templates are generally complicated and eco-unfriendly to machine [22]. Even if they are fabricated, the demolding process after hot embossing is difficult and the most common way is to dissolve Si template in strong alkaline solutions to obtain metallic glass sample [23], which makes the costly Si template a disposable product. Another is that Si templates with optical surface at micro/nanoscale needs more time and extraordinary cost.

In this paper, a neat and low-cost 3D micro dimple arrays thermoplastic microforming method for metallic glasses is introduced. Instead of fabricating a specific Si template with precise 3D microfeatures before embossing, a group of recyclable precision cemented tungsten carbide balls with optical

surface finish and accurate shape were employed as a flexible mold to emboss micro dimples on metallic glass. Compared with the disposable Si template, these cemented tungsten carbide balls could be recycled easily after embossing for next production. Here an example of Zr-based metallic glass ( $Zr_{35}Ti_{30}Cu_{8.25}Be_{26.75}$ ) was applied to demonstrate the whole process of this new embossing method. We proposed a simple two-step method by embossing the metallic glass disk into a plano-concave part and then compressing microballs downward onto the concave surface of metallic glass to produce 3D micro dimple array. Due to gravity and geometry restraint, the balls could be automatically self-aligned into one layer once they were placed on the concave surface. To attain desired 3D micro dimple array on the curved metallic glass surface, accurate processing parameter control such as force and displacement were necessarily required. Accordingly, an FE simulation was then performed to study the material flow behavior in the new method and to determine the relationship between profiles of micro dimples and processing parameters. The profiles of a portion of micro dimple array was extracted from the numerical model and compared with experimental data to indicate that the simulation can serve as guideline in the embossing process. In addition, the 3D microlens array metallic glass mold was eventually evaluated by embossing polymeric compound eye component and then assessing its optical performance, showing that the new mold-free embossing approach we proposed is an effective and cost-saving technique to manufacture 3D micro dimple array on metallic glasses.

## 2 Experiments

### 2.1 BMG Preparation and Characterization

The material used in the paper is Zr based BMG system (Zr–Ti–Cu–Be). These four materials were prepared based on their atomic mass percentage Zr:Ti:Cu:Be = 35:30:8.25:26.75, and subsequently immersed into acetone for ultrasonic cleaning. After washing and drying, the raw materials were placed in an electric arc furnace and melted to uniformly mix into bulk alloy under argon plasma treatment. At last, the molten alloy was drawn into the water-cooled copper mold by the pressure difference between the melting chamber and the copper mold, and cooled at an extremely large speed to form metallic glass sample required for the research. The XRD pattern of the long cylinder metallic glass rod prepared by copper die casting is illustrated in Fig. 1a, indicating that diffraction peaks of crystalline material have not been found, which means that the amorphous metallic glass was well prepared. The original cylindrical surface of metallic glass was rough with pits and weld marks, so a uniform polishing process was

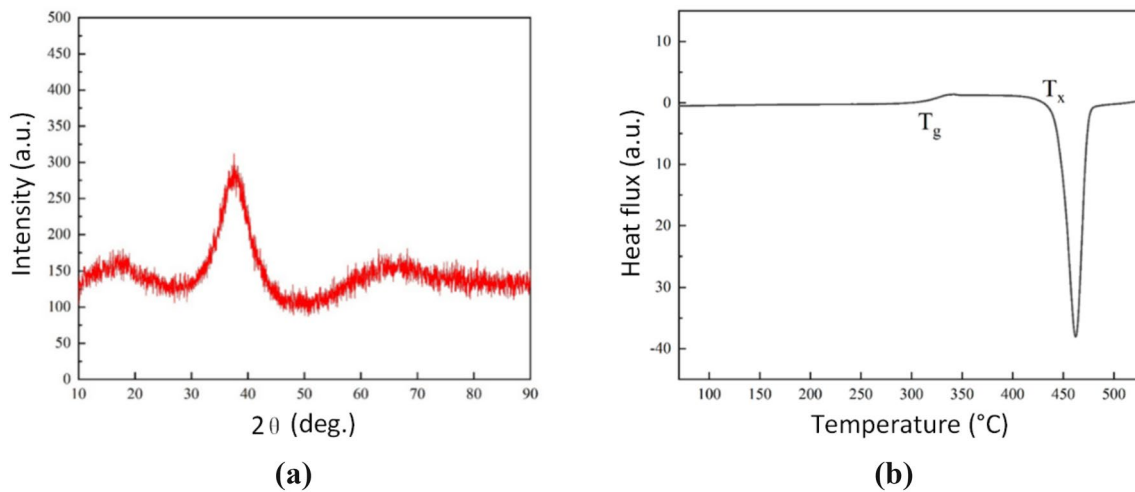


Fig. 1 a The XRD pattern and (b) DSC curve of the metallic glass

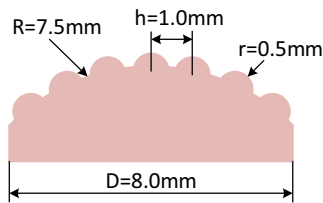


Fig. 2 Design target for 3D microlens array of PMMA

applied to make the surface relatively smooth.  $T_g$  (transition temperature) and  $T_x$  (crystallization temperature) of the metallic glass were measured as 280 °C and 410 °C respectively by reading the DSC (differential scanning calorimetry) curve, as shown in Fig. 1b, leaving a relatively large temperature processing window (130 °C) for hot embossing. In order to fit the sample into the mold sleeves, the cylinder rod was cut with diamond saw into several small disks with diameter of 5 mm and height of 5 mm.

## 2.2 3D Micro Dimple Array Metallic Glass Multi-Ball Hot Embossing Process

In this paper, we intended to fabricate 3D microlens array by creating a 3D micro dimple array mold and then copying the features onto the polymer. The design target for 3D microlens array is as shown in Fig. 2, so a 3D micro dimple array mold with conjugate shape was firstly fabricated. Our newly-developed 3D micro dimple array embossing procedure is similar to the conventional embossing except that a layer of cemented tungsten carbide balls self-aligned on the metallic glass surface is compressed downward to replicate the shape of their spherical crowns instead of a fabricated mold with 3D microlens array

pattern. To fabricate the 3D micro dimple array metallic glass, a self-made precision hot embossing machine was employed. The machine used an electrical servo drive to offer a steady compressing force with capacity of 30 kN and accurate displacement with position error of 1  $\mu\text{m}$ . An infrared lamp and Nitrogen gas purge were applied for rapid heating and cooling of the metallic glass. Specifically, Nitrogen gas was required to aerate throughout the heating and cooling process to avoid the metallic glass and molds being oxidized.

The entire procedure is demonstrated in Fig. 3a. The dimensions and parameters of the mold assembly and balls are listed in Table 1 and the procedure is described as follow: the metallic glass disk was placed in a sleeve with diameter of 8 mm between a flat lower mold and a convex upper mold (To simplify schematic and achieve a clear position relation of mold and metallic glass, sleeve was not given). The metallic glass disk was heated by infrared heater from ambient temperature to embossing temperature (350 °C) and compressed into the plano-concave shape with enlarged diameter of 8 mm and radius of curvature of 7.5 mm. Subsequently, a down displacement of 300  $\mu\text{m}$  with speed of 10  $\mu\text{m/s}$  was applied to the convex stamper to compress self-positioned close-packed balls ( $\varphi = 1\text{mm}$ ) downwards onto the metallic glass surface, which limits the processing time of the hot embossing process within 30 s. Specifically, the speed of 10  $\mu\text{m/s}$  was adopted because a lower speed will reduce the unnecessary deformation of the convex surface of the softened metallic glass and 10  $\mu\text{m/s}$  is the speed limit of the home-made hot embossing machine. After reaching the pre-set displacement, the setup was quickly cooled down to room temperature and balls were removed to obtain the 3D micro dimple array.

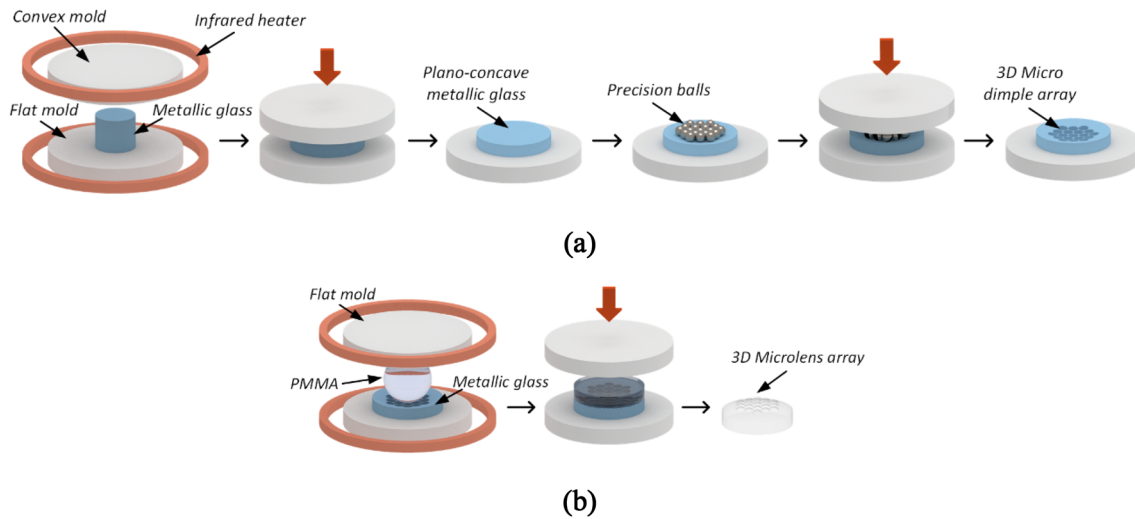


**Fig. 3** Experimental processes of (a) 3D micro dimple array fabrication on metallic glass and (b) 3D microlens array fabrication on PMMA

**Table 1** Dimensions and parameters of the mold assembly and ball

Parameters	Upper mold	Lower mold	Mold sleeve	Microball
Sketch				
Height $H$ (mm)	10.00	5.05	14.50	
Diameter $D$ (mm)	8.0	8.0	$D_1=8.0$ , $D_2=10.0$	1.0
Curvature $R$ (mm)	7.5			
Surface roughness $R_a$ (nm)	6.4	22.1	27.6	7.9
Material	Stainless steel	Stainless steel	Stainless steel	Cemented tungsten carbide

### 2.3 3D PMMA Microlens Array Molding Process

A 3D PMMA microlens array was fabricated, as shown in Fig. 3b. The spherical PMMA and metallic glass mold were firstly heated to 150 °C, and then a velocity of 10  $\mu\text{m/s}$  was applied to lower molds to compress softening PMMA upward into micro features to achieve

complete filling under molding pressure of 2.5 kN. After that, a small cooling rate of 0.05 °C/s was adopted to minimize the residual stresses and refractive index deviation in the microlens array caused by the large deformation and temperature changes in hot embossing process. Finally, the PMMA micro part was released at 50 °C and cooled in open air to 25 °C.

### 3 Multi-Ball Hot Embossing FEM Simulations

#### 3.1 Heat Transfer Model of Multi-Ball Hot Embossing

Metallic glass hot embossing process usually requires stable and constant molding temperature because the flow behavior and thermo-plastic deformation of metallic glass varies dramatically with temperature in its supercooled liquid region. Instead of material completely filled into micro cavities, our new method enables material flow around balls and be squeezed by balls to form micro dimples and gaps, which means the temperature change of the metallic glass and its material flow behaviors at various temperatures can greatly affect the accuracy of shape profiles in micro dimples. However, the temperature change measurement inside metallic glass could be extremely difficult. Therefore, as shown in Fig. 4, modeling of heat transfer phenomenon in multi-ball metallic glass hot embossing process was conducted to express the heat transfer calculation in FEM simulation, thereby investigating the material flow behaviors under different temperatures in multi-ball hot embossing.

Firstly, the heat transfer between the molds and the metallic glass was investigated. As shown in Fig. 4, mold assembly are mainly heated by thermal convection from the flowing nitrogen gas to the mold, and thermal radiation from infrared lamp, while the thermal conduction from molds is the primary contribution to the temperature rise

of metallic glass. The thermal boundary conditions of the metallic glass can be expressed as [24]:

$$-k_T \frac{\partial T}{\partial l} = h_m(T - T_m) \tag{1}$$

where  $k_T$  is thermal conductivities of metallic glass under various temperatures.  $h_m$  is the heat transfer coefficient from the molds to metallic glass, which can be described as function of interface pressure, surface roughness and temperature [25].  $T_m$  is mold temperature acquired by thermocouples.

Next, we study the heat conduction between sphere and metallic glass. The contact thermal conductance between each sphere and plane  $h_i$  can be simplified as [26]:

$$h_i = \frac{2\sqrt{Rd}\lambda_s}{\left(1 - \sqrt{\frac{d}{R}}\right)^{\frac{3}{2}}} \tag{2}$$

where  $d$  is the elastic depth of ball, and can be expressed as  $d = \left(\frac{3F}{4E^*R^{\frac{1}{2}}}\right)^{\frac{2}{3}}$ ,  $R$  is the radius of the ball,  $\lambda_s$  is the heat transfer coefficient. The number of balls is  $N$ , the total contact thermal resistance  $h$  can be expressed as:

$$h = \sum_{i=1}^N h_i \tag{3}$$

Eventually, the heat transfer within the metallic glass was considered. Since the metallic glass was simultaneously heated by mold sleeve, upper mold, lower mold and balls, temperature field of the metallic glass material requires time

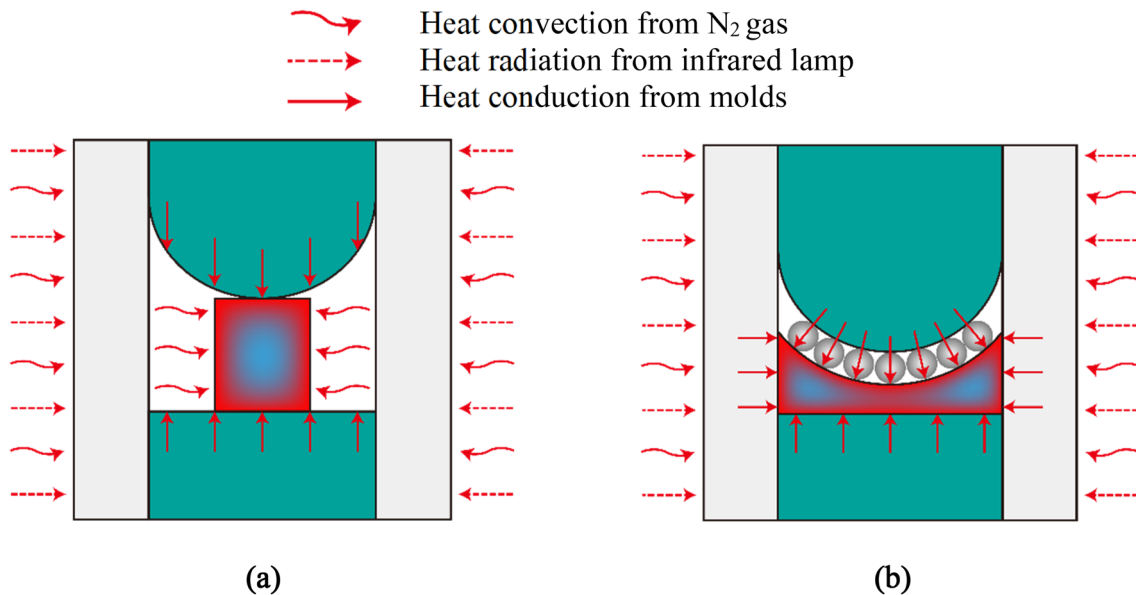


Fig. 4 Schematic of three heat transfer modes during (a) concave surface hot embossing process and (b) multi-ball hot embossing process

to be even. The governing equation for heat transfer in metallic glass can be expressed as:

$$\rho C_p \frac{\partial T}{\partial t} = k \nabla^2 T \quad (4)$$

where  $\rho$ ,  $C_p$ , and  $k$  are the density, specific heat, and thermal conductivity of metallic glass, respectively.

### 3.2 Material Flow Model of Metallic Glass

Researchers have constructed several constitutive models to quantitatively describe the steady-state flow behavior of metallic glasses in the supercooled liquid region [27–29]. Among these models, although the virtual stress model based on stress relaxation has deviation in describing the stress overshoot of metallic glasses, it exhibits good performance in terms of the steady state flow behavior under the Newton and non-Newtonian flow states [30]. The steady-state flow viscosity of metallic glass can be expressed by the ratio of steady-state flow stress to strain rate, expressed as:

$$\eta_f = \frac{\sigma_{\text{flow}}}{3\dot{\epsilon}} \quad (5)$$

where  $\sigma_{\text{flow}}$  is flow stress in steady state and  $\dot{\epsilon}$  is strain rate.

The Newtonian viscosity of the supercooled liquid region of the metallic glass can be expressed by the Arrhenius relationship:

$$\eta_N = B \exp\left(\frac{H}{RT}\right) \quad (6)$$

where  $B$  is the structure parameter,  $H$  is the viscous activation energy,  $R$  is the gas constant.

For the metallic glass in a steady-state flow state, the stress relaxation time  $\lambda_N$  is generally considered to be proportional to the steady-state flow viscosity  $\eta_f$  of the amorphous alloy, so the stress relaxation process can be expressed as:

$$\frac{\eta_f}{\eta_N} = \frac{\lambda_f}{\lambda_N} = 1 - \exp\left(-\frac{1}{t\alpha_T\dot{\epsilon}}\right) \quad (7)$$

$$\alpha_T = A \exp\left(\frac{H^*}{RT}\right) \quad (8)$$

where  $\alpha_T$  is the conversion factor,  $A$  is the structure parameter,  $H^*$  is the activation energy corresponding to the conversion factor.

Therefore, the virtual stress model of steady flow stress in metallic glass can be expressed as:

$$\sigma_{\text{flow}} = 3\dot{\epsilon}B \exp\left(\frac{H}{RT}\right) \left[ 1 - \exp\left(\frac{-1}{tA \exp\left(\frac{H^*}{RT}\right)\dot{\epsilon}}\right) \right] \quad (9)$$

### 3.3 FEM Simulation

A 2D FE simulation of the single ball embossing on a plane metallic glass surface was firstly performed using MSC. Marc software to investigate the material flow behavior around ball under different temperatures in supercooled liquid region. As illustrated in Fig. 5a, the metallic glass disk was fixed and the single cemented tungsten carbide ball placed above was driven downward to press the metallic glass into a dimple with a constant velocity. To accord

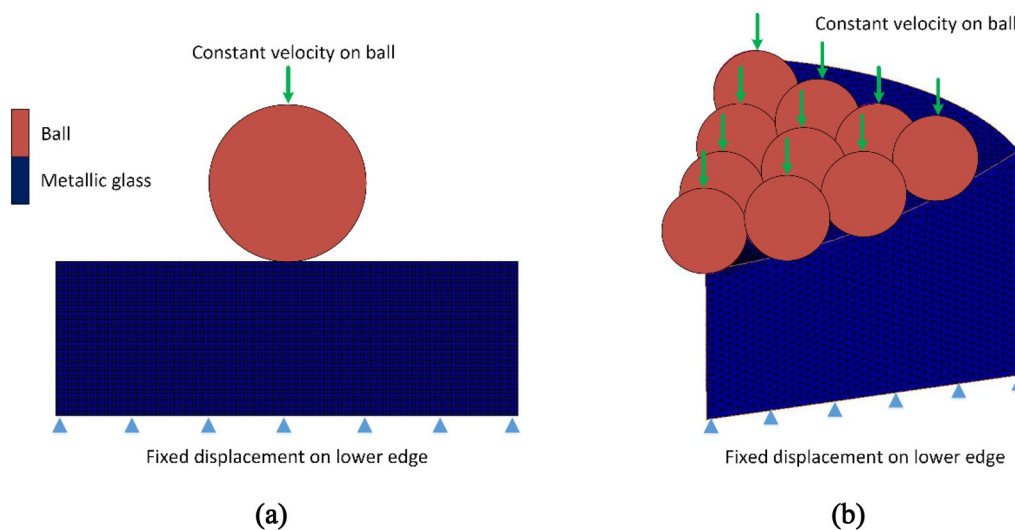


**Fig. 5** (a) 2D FEM model for single ball embossing on plane metallic glass and (b) One-sixth 3D FEM molding model for multi-ball embossing on curved metallic glass

with the experiment, the Young’s modulus, Poisson’s ratio and density of the metallic glass were set as 31.8 GPa, 0.37 and 5.19 g/cm<sup>3</sup>, respectively, based on its material properties [31]. In this model, the ball and metallic glass were defined as rigid and deformable bodies, respectively. The simulation was carried out by applying true stress-true strain curves under different temperatures onto the metallic glass then cooled to room temperature.

In addition, since multi-ball embossing on a curved surface will be an extremely complicated problem and the real depth of micro dimples can be influenced by surrounding balls and difficult to predict, a 3D FE simulation of the multi-ball embossing process was also performed using MSC.Marc software, which was compared with experimental data subsequently to validate its feasibility. As shown in

Fig. 5b, a one-sixth centrosymmetric model was established using one-sixth of entire balls and a plano-concave metallic glass solid, which were modeled as rigid bodies and deformable body discretized into 316,400 tetrahedral four-node elements, respectively.

## 4 Results and Discussion

### 4.1 Geometrical Morphology Evaluation

The 3D micro dimple array fabricated by the novel self-aligned multi-ball embossing method was presented in Fig. 6a and its corresponding 3D microlens arrays molded

**Fig. 6** The photographs of (a) the 3D micro dimple array on metallic glass, (b) the corresponding 3D microlens array duplicated on polymer

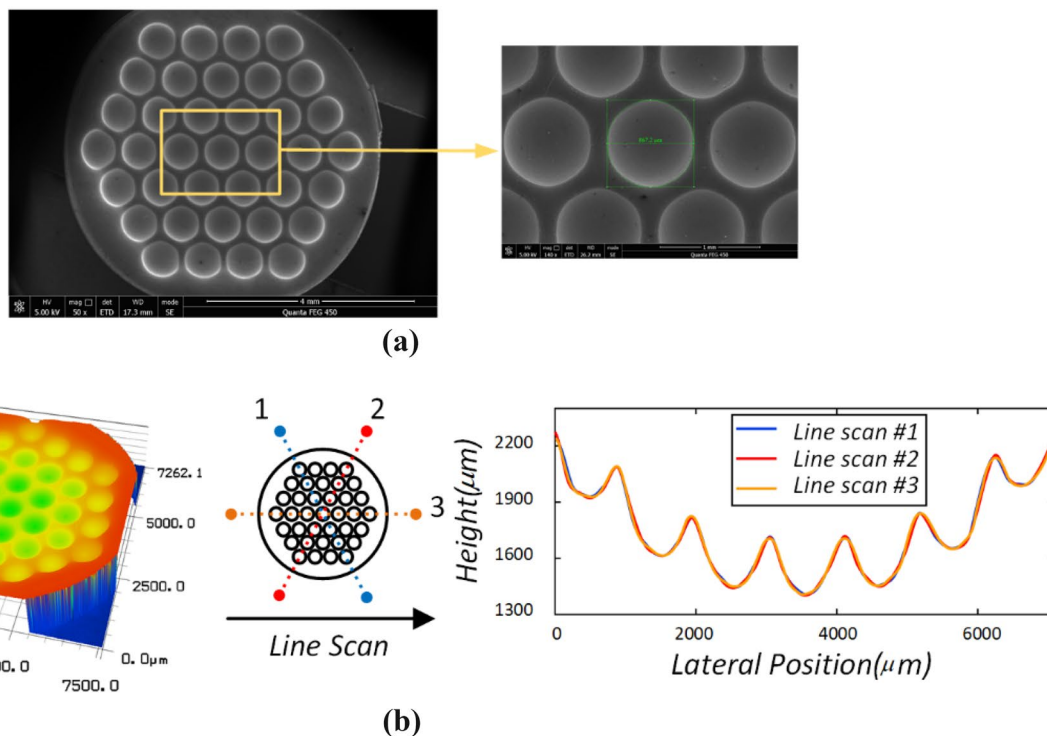
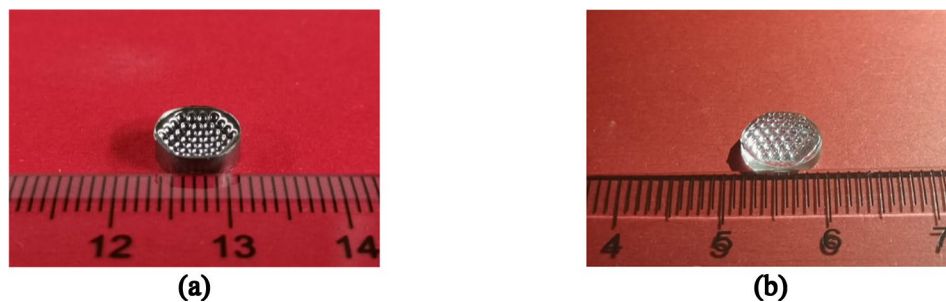


**Fig. 7** a SEM image of the 3D metallic glass micro dimple array and the magnification of the center micro dimple with the aperture measurement. b 3D morphology of the micro dimple array and surface profiles at three equally spaced radial sections

using PMMA are illustrated in Fig. 6b. No visible dirt or other surface defects was discovered on the metallic glass.

Figure 7a presents SEM images of the metallic glass micro dimple array from the top view, showing clear and circular micro dimples and an even gap width between each micro dimple. Even though balls were flexibly worked as mold in the embossing, the positioning of each micro dimple can still be accurately guaranteed by the close-packed self-aligned ball array on the concave surface. To quantitatively evaluate the surface profiles of micro dimples, the centered micro dimple was set as target. The measured aperture is  $867.2\ \mu\text{m}$ , the sag height at the dimple vertex is  $416.8\ \mu\text{m}$ , and the pitch between micro dimples is  $172.1\ \mu\text{m}$ . Further and detailed geometry characterization was implemented for entire array by laser scanning confocal microscope (KEYENCE VK-250), and the surface morphology is shown in Fig. 7b. According to the centrosymmetric micro dimple array pattern, the surface profile data at three equally spaced radial sections were extracted and compared. These profiles seem to be quite identical to each other, which demonstrates a precision distribution of the embossed metallic glass micro dimple array. In addition, the surface roughness and replication fidelity of embossed micro dimples were also identified by a non-contact profilometer (Bruker Contour GTX). As presented in Fig. 8a, b, no notable differences were found between the surfaces of the embossing ball and the micro dimple. The surface roughnesses of the ball and dimple were measured as  $7.9\ \text{nm}$  and  $8.2\ \text{nm}$ , respectively, showing an excellent inheritance from flexible mold surface to embossed surface in surface roughness during the embossing process.

## 4.2 Material Flow Behavior in Multi-Ball Embossing

Due to the thermo-plasticity of metallic glass, material around each ball will be deformed upwards into pile-ups in different shapes during ball pressing, which causes that the down displacement of ball  $h$  does not equal to the depth of micro dimple  $h_c$ , thereby requiring a one-to-one relationship between  $h_c$  and  $h$  to guide the process. Hence, a 2D

single ball hot embossing model was initially constructed and to simulate the micro dimple profile of single dimple on the plane metallic glass surface. A down displacement of  $300\ \mu\text{m}$  was applied on ball at velocity of  $10\ \mu\text{m/s}$  to compress the softening metallic glass at  $370\ ^\circ\text{C}$ , as shown in Fig. 9a. In addition, the profile shapes of micro dimples under the same down displacement and temperatures of  $330\ ^\circ\text{C}$ ,  $340\ ^\circ\text{C}$ ,  $350\ ^\circ\text{C}$ ,  $360\ ^\circ\text{C}$ , and  $370\ ^\circ\text{C}$  are plotted in Fig. 9b. We noticed that with the increase of temperature, the pile-up material gradually decreases, thereby  $h_c/h$  correspondingly drops. This is mainly because the higher temperature leads to lower viscosity, which makes the response speed of the atomic arrangement in the metallic glass faster, and a stable Newtonian fluid state easier to reach.

To investigate the complex material flow behavior in multi-ball embossing on curved surface, different stages ( $h = 100\ \mu\text{m}$ ,  $200\ \mu\text{m}$ ,  $300\ \mu\text{m}$ ) of material deformations with cross-sectional contours of micro dimples during embossing process were presented in Fig. 10a–c. It can be clearly concluded that thermoplastic metallic glass in super-cooled liquid region tends to form pile-up around balls based on its constitutive equation. With the increase of  $h$ , un conspicuous pile-ups formed around balls gradually become larger and move towards each other, leading to the material sandwiched between balls is nearly in concave shape with obvious pile-ups on both sides. As the compressing continues, the pile-ups around each ball keep gathering towards the middle and finally the material sandwiched between balls is squeezed into a narrow region with two spherical surfaces and an almost flat tip. Consequently, with the help of the FE model,  $h_c$  corresponding to each  $h$  in different stages can be easily calculated as  $132\ \mu\text{m}$ ,  $250\ \mu\text{m}$ ,  $409\ \mu\text{m}$ . To clearly find out the profile evolution of micro dimples on curved surface during multi-ball pressing, the contours of metallic glass under different down displacements were extracted and plotted in Fig. 11. We can conclude that as balls Apart from morphology evolution resulted from material flow, Von Mises pressure distribution of micro dimples in three

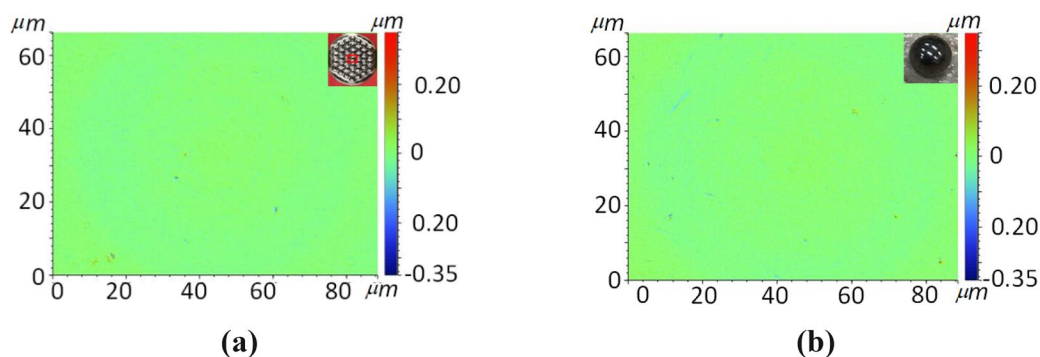


Fig. 8 Surface roughness image of (a) the center micro dimple and (b) the embossing ball

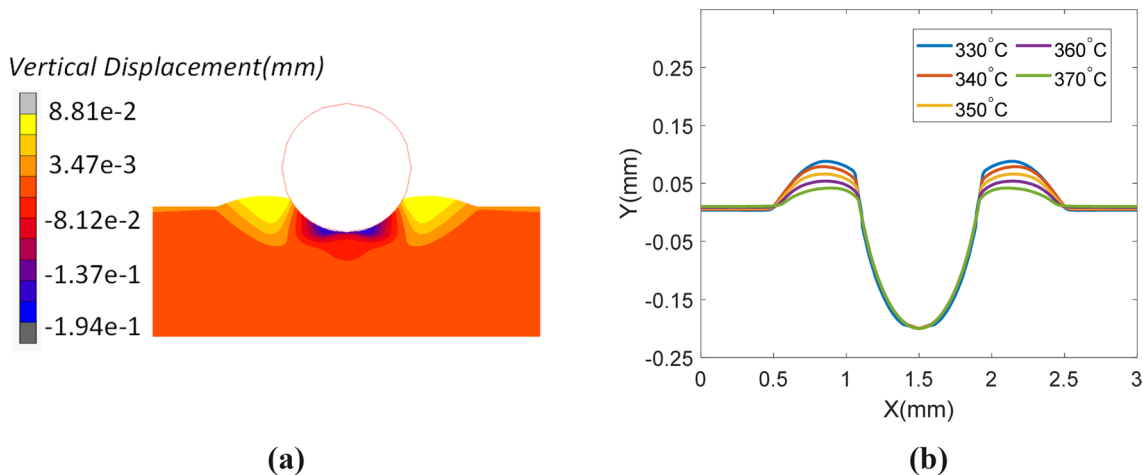


Fig. 9 a Vertical displacement distribution in the metallic glass at molding temperature of 370 °C, (b) Profile shapes of the micro dimple at various temperatures of 330 °C, 340 °C, 350 °C, 360 °C, and 370 °C

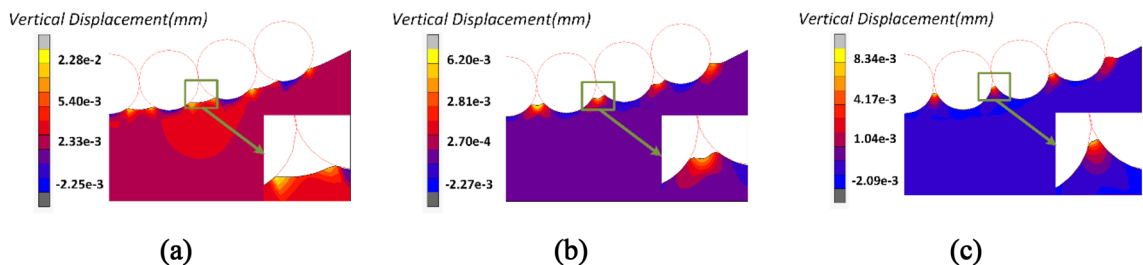


Fig. 10 a–c Cross-sectional contours of metallic glass when ball vertical displacement of 100 μm, 200 μm, 300 μm are applied

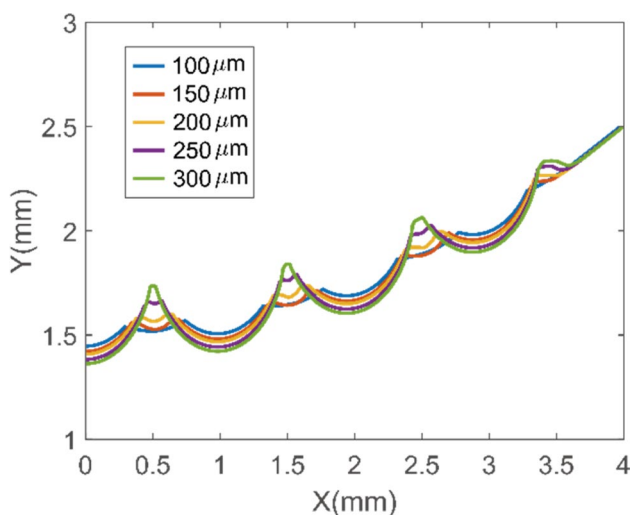


Fig. 11 Cross-sectional contours of metallic glass when ball vertical displacement of 100 μm, 150 μm, 200 μm, 250 μm, 300 μm are applied

different stages ( $h = 100 \mu\text{m}, 200 \mu\text{m}, 300 \mu\text{m}$ ) were also investigated, as shown in Fig. 12a, c. It is clear from the figure that the high stress zone is distributed in or close to each micro dimple. The localized stress distribution at the bottom of dimples strengthens the material flow of metallic glass during ball compressing and facilitates the rapid shape forming of micro dimples.

To validate the FE model, a down displacement of 300 μm was applied on the FE model and the cross-sectional contour of a portion of micro dimples was extracted and compared with the experimental data in Fig. 13, which indicates a good agreement between simulation and experiment. Particularly, we noticed that the profiles of dimples close to the center present a better agreement with experimental data than that away from the center. We presumed that the possible reason may be that the outer balls slightly move towards outside since the friction force between balls and stamper is not sufficient large during hot embossing process.

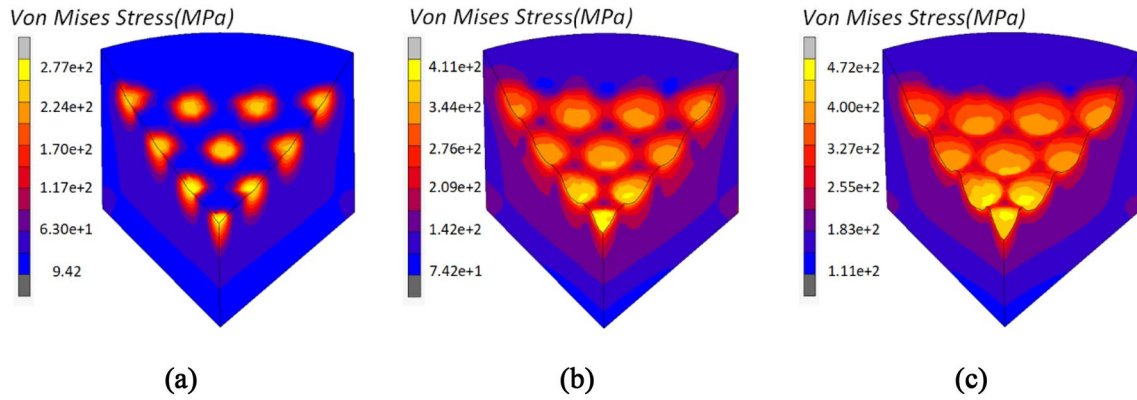


Fig. 12 a–c Von Mises stress distribution of metallic glass when ball vertical displacement of 100 μm, 200 μm, 300 μm are applied

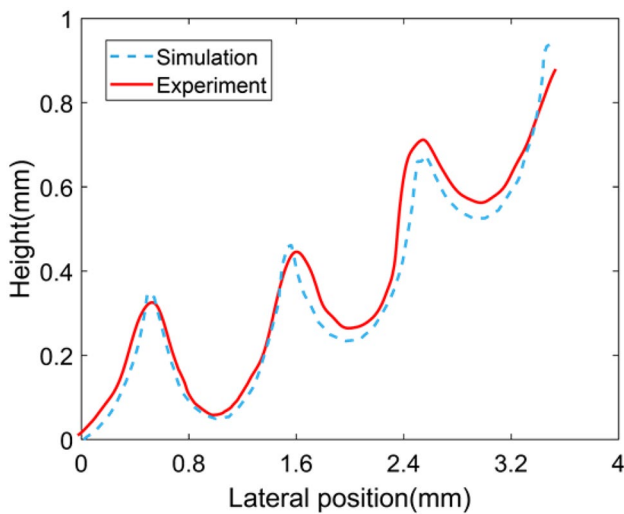


Fig. 13 Comparison of cross-sectional contour after embossing between simulation and experiment

### 4.3 Position Prediction Model of Micro Dimple Array

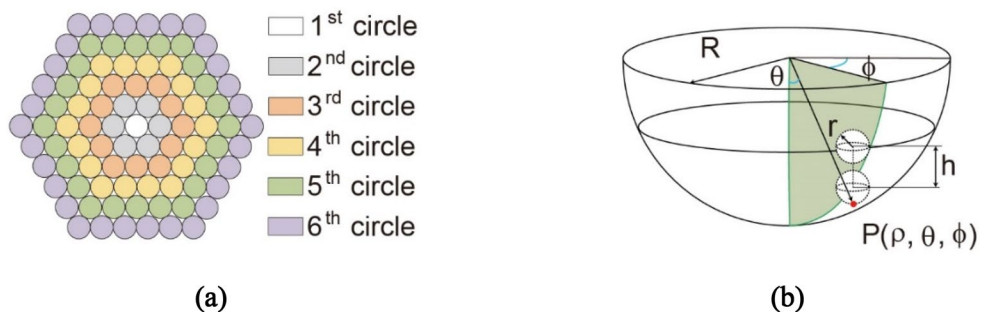
Instead of regular square array, the self-aligned multi-ball embossing method proposed in this paper has its specific pattern distribution. Benefited from gravity and geometric

constraint, balls can be self-aligned as one layer on a concave surface according to one layout. In this layout, balls are stably positioned one by one in integral number of circles, as illustrated in Fig. 14a. To ensure symmetry of balls and avoid unbalance force during compressing, balls have to be patterned in integral number of circles such as a pattern with 4 circles demonstrated in the paper. The process of the proposed method can be described as follow: Balls with radius of  $r$  are placed on the concave spherical surface with radius of curvature of  $R$  and then vertically down pressed by a displacement of  $h$  into the surface. As shown in Fig. 14b, this section can provide spherical coordinates of each micro dimple vertex as follow through the calculation of geometry relationship among these balls.

$$\text{For circle } n = 1 : P(\rho, \theta, \varphi) = (R + h, 0, 0) \tag{10}$$

$$\text{For circle } n = 2 : P(\rho, \theta, \varphi) = \begin{cases} \rho = \sqrt{l_1^2 + (l_2 + h + r)^2} \\ \theta = \arctan \frac{l_1}{l_2 + h + r} \\ \varphi = \frac{(i - 1)\pi}{3} \end{cases} \tag{11}$$

Fig. 14 a Schematic of self-aligned ball in circles. b Schematic of moving path of a random ball in spherical coordinates



$$\text{For circle } n = 3 : P_1(\rho, \theta, \varphi) = \begin{cases} \rho = l_3 = \sqrt{l_1^2 + (l_2 + h + r)^2} \\ \theta = \arctan \frac{l_1}{l_1 + h + r} \\ \varphi = \frac{(i-1)\pi}{3} \end{cases} \quad (\text{Condition 1}) \quad (12)$$

$$P_2(\rho, \theta, \varphi) = \begin{cases} \rho = l_3 = \sqrt{l_1^2 + (l_2 + h + r)^2} \\ \theta = \arctan \frac{l_1}{l_1 + h + r} \\ \varphi = \frac{\pi}{6} + \frac{(i-1)\pi}{3} \end{cases} \quad (\text{Condition 2}) \quad (13)$$

$$P_2(\rho, \theta, \varphi) = \begin{cases} \rho = l_3 = \sqrt{l_1'^2 + (l_2 + h + r)^2} \\ \theta = \arctan \frac{l_1'}{l_1 + h + r} \\ \varphi = \frac{\pi}{6} + \frac{(i-1)\pi}{3} \pm \gamma \end{cases} \quad (\text{Condition 2}) \quad (15)$$

where  $i = 1 \sim 6$ . The other variables including  $l_1, l_1', l_2$  and  $l_3$  are simple expressions for  $\alpha, \beta, \delta, r, R, h_1$ , which are pre-

$$\text{For circle } n = 4 : P_1(\rho, \theta, \varphi) = \begin{cases} \rho = l_3 = \sqrt{l_1^2 + (l_2 + h + r)^2} \\ \theta = \arctan \frac{l_1}{l_1 + h + r} \\ \varphi = \frac{(i-1)\pi}{3} \end{cases} \quad (\text{Condition 1}) \quad (14)$$

sented in Fig. 15. By implementing this methodology, the position distribution of each micro dimple on concave surface can be accurately obtained, which can as well facilitate

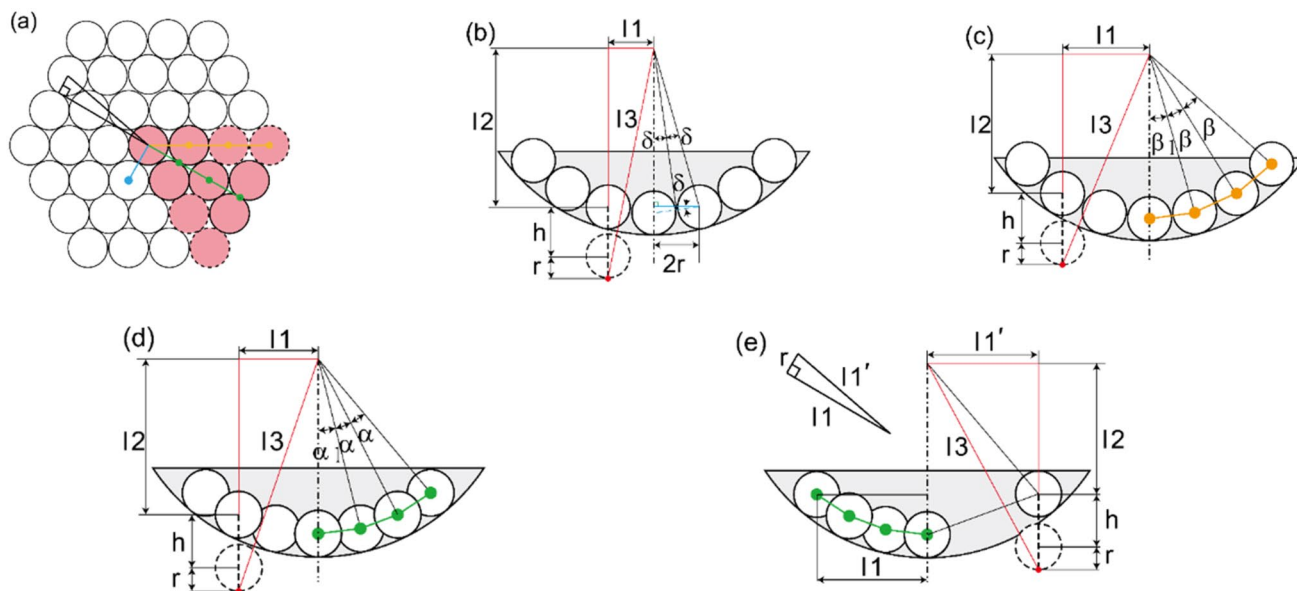
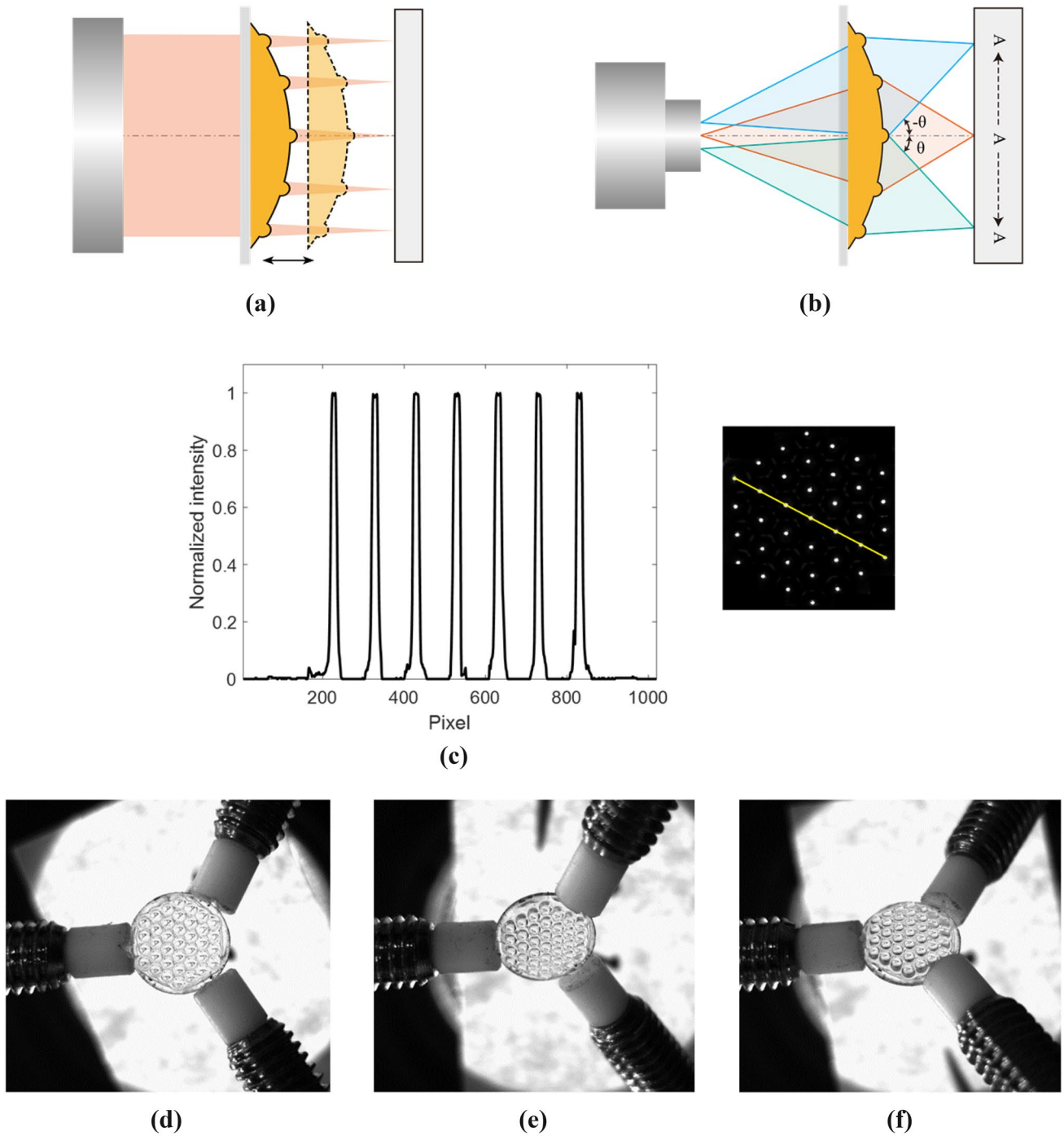


Fig. 15 a Sketch of ball layout from top view. b–e Different cross-sectional sketches of relative positions of balls according to four lines in (a)



**Fig. 16** **a** Schematic of the optical setup for measuring focus point. **b** Schematic of the optical setup for measuring imaging capacity. **c** Intensity data and image of the focus points of 3D PMMA microlens

array from a CCD camera. **d–f** Imaging photographs of **(b)** Presenting capital letter 'A' at three various angles of  $-40^\circ$ ,  $0^\circ$  and  $40^\circ$

quick estimation of position distribution of microlens array on conjugate polymer.

#### 4.4 Optical Test of 3D Microlens Array

The optical performance of 3D microlens array including focusing and imaging functions was also tested. A beam of parallel light was projected to the 3D PMMA microlens array to achieve its focus point image by adjusting the sample to its focus length, as shown in Fig. 16a. Consequently, the intensity of seven microlenses on the diagonal of the entire hexagonal array pattern are demonstrated as Fig. 16c with the focus point image on its top left corner. The normalized light intensities of seven microlenses were captured and calculated as 0.991, 0.982, 0.989, 0.979, 0.992, 0.990 and 0.985, respectively, showing that the fabricated PMMA compound eye has a perfect focusing function with uniform spot intensity.

3D microlens arrays are superior to microlens array on flat surface in capturing larger FOV (field of view) because individual lenlets of compound eye structure are capable of imaging omni-directionally in the space. To evaluate the FOV and imaging performance of the 3D PMMA microlens array, another optical system was built as shown in Fig. 16b. The imaging system consisted of a target (screen with a capital letter 'A'), the PMMA sample, a rotational stage with accurate angle measurement and a CCD camera. The PMMA sample was fixed on the rotational stage, where the angle between light source and the PMMA compound eye could be adjusted. During the measuring process, a black capital letter 'A' was projected through the PMMA microlens array, and the microlens array could be rotated from center to both sides for CCD camera to capture different letter images at different incident angles. The results show that each microlens can form a tiny yet clear 'A' image on the CCD camera when  $-40^\circ \leq \theta \leq 40^\circ$ , which are presented in Fig. 16d–f. By contrast, when  $\theta > 40^\circ$  or  $\theta < -40^\circ$ , capital letter 'A' can still be captured but starts to blur because the 'A' has been moved out of the focal plane with the increase of incident angle. Therefore, we can roughly speculate that the 3D PMMA microlens array with a FOV of about  $80^\circ$  can be achieved in high-volume.

## 5 Conclusions

In summary, this paper demonstrates a green and rapid self-aligned multi-ball embossing approach for the 3D fabrication of metallic glass micro dimple arrays by adopting stampers with spherical surfaces and a group of recyclable cemented tungsten carbide precision balls. A four-circle micro dimple array with aperture of  $867.2 \mu\text{m}$  was successfully fabricated

with optical surface finish (8.2 nm) and perfect uniformity in 30 s. The morphology evolution of micro dimples under different ball displacements were then revealed by a verified FE model. Moreover, the PMMA compound eye structure was eventually embossed with a large FOV (no less than  $80^\circ$ ) and uniform focus point distribution. The process developed in the paper provides great potentials for various applications such as ultra-HD imaging and machine vision, and offers instructive inspirations for high-volume fabrication with large demands for 3D metallic glasses microlens array mold.

**Acknowledgements** The authors gratefully acknowledge the financial support of the National Key Research and Development Program of China (2018YFA0703605) and Natural Science Foundation of Guangdong Province (2018A030313466).

#### Compliance with ethical standards

**Conflict of interest** On behalf of all authors, the corresponding author states that there is no conflict of interest.

## References

- Hofmann, D. C., Suh, J. Y., Wiest, A., Duan, G., Lind, M. L., Demetriou, M. D., et al. (2008). Designing metallic glass matrix composites with high toughness and tensile ductility. *Nature*, *451*(7182), 1085–1089.
- Huang, Y., Guo, Y., Fan, H., & Shen, J. (2012). Synthesis of Fe–Cr–Mo–C–B amorphous coating with high corrosion resistance. *Materials Letters*, *89*, 229–232.
- Li, M. X., Zhao, S. F., Lu, Z., Hirata, A., Wen, P., Bai, H. Y., et al. (2019). High-temperature bulk metallic glasses developed by combinatorial methods. *Nature*, *569*(7754), 99–103.
- Klement, W., Willens, R. H., & Duwez, P. (1960). Non-crystalline structure in solidified gold-silicon alloys. *Nature*, *187*(4740), 869–870.
- Yao, D., Deng, L., Zhang, M., Wang, X., Tang, N., & Li, J. (2015). A size-dependent constitutive model of bulk metallic glasses in the supercooled liquid region. *Scientific reports*, *5*, 8083.
- Kumar, G., Tang, H. X., & Schroers, J. (2009). Nanomoulding with amorphous metals. *Nature*, *457*(7231), 868–872.
- Wang, X., Dai, W., Zhang, M., Gong, P., & Li, N. (2018). Thermo-plastic micro-formability of TiZrHfNiCuBe high entropy metallic glass. *Journal of Materials Science & Technology*, *34*(11), 2006–2013.
- Lee, S. H., Kim, S. W., Park, C. W., Jeong, H. E., Ok, J. G., & Kwak, M. K. (2017). Scalable fabrication of flexible transparent heaters comprising continuously created metallic micromesh patterns incorporated with biomimetic anti-reflection layers. *International Journal of Precision Engineering and Manufacturing-Green Technology*, *4*(2), 177–181.
- Li, R., Liu, X. J., Wu, R. Y., Wang, J., Li, Z. B., Chan, K. C., et al. (2019). Flexible honeycombed nanoporous/glassy hybrid for efficient electrocatalytic hydrogen generation. *Advanced Materials*, *31*(49), 1904989.
- Ida, I., Seiryu, M., Takeshita, N., Iwasaki, M., Yokoyama, Y., Tsutsumi, Y., et al. (2018). Biosafety, stability, and osteogenic

- activity of novel implants made of Zr70Ni16Cu6Al8 bulk metallic glass for biomedical application. *Acta biomaterialia*, 74, 505–517.
11. Liu, X., Shao, Y., Tang, Y., & Yao, K. F. (2014). Highly uniform and reproducible surface enhanced raman scattering on air-stable metallic glassy nanowire array. *Scientific reports*, 4, 5835.
  12. Lee, H.-J., & Park, K. (2014). Development of composite micro-patterns on polymer film using repetitive ultrasonic imprinting. *International Journal of Precision Engineering and Manufacturing-Green Technology*, 1(4), 341–345.
  13. Moon, B. J., Kim, J., & Lee, S. K. (2015). Suppression of thermal crown of heating roll for large area thermal imprint with consideration of thermal resistance between roll and shaft. *International Journal of Precision Engineering and Manufacturing-Green Technology*, 2(4), 315–323.
  14. Bae, H., & Park, K. (2016). Design and analysis of ultrasonic horn for polymer sheet forming. *International Journal of Precision Engineering and Manufacturing-Green Technology*, 3(1), 49–54.
  15. Moon, I. Y., Kim, B. H., Lee, H. W., Oh, Y. S., Kim, J. H., & Kang, S. H. (2020). Superhydrophobic polymer surface with hierarchical patterns fabricated in hot imprinting process. *International Journal of Precision Engineering and Manufacturing-Green Technology*, 7(2), 493–503.
  16. Xu M, Zhou Z, Wang Z, Lu H Self-assembled microlens array with controllable focal length formed on a selective wetting surface. *ACS Applied Materials & Interfaces*, 2020.
  17. Busch, R., Bakke, E., & Johnson, W. L. (1998). Viscosity of the supercooled liquid and relaxation at the glass transition of the Zr46.75Ti8.25Cu7.5Ni10Be27.5 bulk metallic glass forming alloy. *Acta Materialia*, 46(13), 4725–4732.
  18. Zhang, N., Srivastava, A. P., Browne, D. J., & Gilchrist, M. D. (2016). Performance of Nickel and bulk metallic glass as tool inserts for the microinjection molding of polymeric microfluidic devices. *Journal of Materials Processing Technology*, 231, 288–300.
  19. Liu, X., Shao, Y., Lu, S. Y., & Yao, K. F. (2015). High-accuracy Bulk metallic glass mold insert for hot embossing of complex polymer optical devices. *Journal of Polymer Science Part B*, 53(7), 463–467.
  20. Ma, J., Zhang, X., & Wang, W. H. (2012). Metallic glass mold insert for hot embossing of polymers. *Journal of Applied Physics*, 112(2), 024506.
  21. Saotome, Y., Imai, K., Shioda, S., Shimizu, S., Zhang, T., & Inoue, A. (2002). The micro-nanoformability of pt-based metallic glass and the nanoforming of three-dimensional structures. *Intermetallics*, 10(11–12), 1241–1247.
  22. Mukaida, M., & Yan, J. (2017). Ductile machining of single-crystal silicon for microlens arrays by ultraprecision diamond turning using a slow tool servo. *International Journal of Machine Tools and Manufacture*, 115, 2–14.
  23. Schroers, J., Nguyen, T., O’Keeffe, S., & Desai, A. (2007). Thermoplastic forming of bulk metallic glass—applications for mems and microstructure fabrication. *Materials Science and Engineering*, 449, 898–902.
  24. Yan, J., Zhou, T., Masuda, J., & Kuriyagawa, T. (2009). Modeling high-temperature glass molding process by coupling heat transfer and viscous deformation analysis. *Precision Engineering*, 33(2), 150–159.
  25. Yi, A. Y., & Jain, A. (2005). Compression molding of aspherical glass lenses-A combined experimental and numerical analysis. *Journal of the American Ceramic Society*, 88(3), 579–586.
  26. Cooper, M. G., Mikic, B. B., & Yovanovich, M. M. (1969). Thermal contact conductance. *International Journal of heat and mass transfer*, 12(3), 279–300.
  27. Johnson, W., and Samwer, K.J.P.r.l., A universal criterion for plastic yielding of metallic glasses with a  $(T/T_g)^{2/3}$  temperature dependence, 95(19): 195501, 2005.
  28. Ekambaram, R., Thamburaja, P., Yang, H., Li, Y., and Nikabdullah, N., “The Multi-axial Deformation Behavior of Bulk Metallic Glasses at High Homologous Temperatures”, Vol. 47, No. 5, pp. 678–690, 2010
  29. Jun, H. J., Lee, K. S., Yoon, S. C., Kim, H. S., & Chang, Y. W. (2010). Finite-element analysis for high-temperature deformation of bulk metallic glasses in a supercooled liquid region based on the free volume constitutive model. *Acta materialia*, 58(12), 4267–4280.
  30. Wang, C., Cheng, S., Ma, M., Shan, D., & Guo, B. (2016). A Maxwell-extreme constitutive Model of Zr-based bulk metallic glass in supercooled liquid region. *Materials & Design*, 103, 75–83.
  31. Duan, G., Wiest, A., Lind, M.L., Li, J., Rhim, Won-Kyu, and Johnson, W.L. “Bulk Metallic Glass with Benchmark Thermoplastic Processability”, *Advanced Materials*, Vol. 19, No. 23, pp. 4272–4275, 2007.

**Publisher’s Note** Springer Nature remains neutral with regard to jurisdictional claims in published maps and institutional affiliations.



**Xiaohua Liu** is a postdoctor in College of Mechatronics and Control Engineering at Shenzhen University. She received her PhD degree in mechanical engineering from Beijing Institute of Technology in 2019. Her main research directions include micro/nano forming and graphene coating.



**Ruodong Mo** is a master in College of Mechatronics and Control Engineering at Shenzhen University. His main research focuses on metallic glass.



**Kangsen Li** is a PhD candidate in College of Mechatronics and Control Engineering at Shenzhen University. His main research focuses on glass molding.



**Jiang Ma** is an associate professor in College of Mechatronics and Control Engineering at Shenzhen University. He received his PhD degree in condensed physics from Institute of Physics, Chinese Academy of Science in 2014. His research interests include micro forming of metallic glasses, ultrasonic forming of metallic materials and their applications.



**Jun Shen** is a Professor in College of Mechatronics and Control Engineering at Shenzhen University. He received his PhD degree in material processing engineering from Harbin Institute of Technology in 1993. His research interests include metallic glasses and additive manufacturing.



**Feng Gong** is a Professor in College of Mechatronics and Control Engineering at Shenzhen University. He received his PhD degree in material processing engineering from Harbin Institute of Technology in 2010. His current research focuses on glass molding and micro forming.